Probing the Nucleus Model for Oligomer Formation during Insulin Amyloid Fibrillogenesis

Leonard F. Pease III,[†‡][*] Mirco Sorci,[§] Suvajyoti Guha,[†¶] De-Hao Tsai,[†¶] Michael R. Zachariah,[†¶] Michael J. Tarlov,[†] and Georges Belfort[§][*]

[†]National Institute of Standards and Technology, Gaithersburg, Maryland; [‡]Departments of Chemical Engineering, Pharmaceutics & Pharmaceutical Chemistry, and Gastroenterology, University of Utah, Salt Lake City, Utah; [§]Department of Chemical and Biological Engineering, and The Center for Biotechnology and Interdisciplinary Studies, Rensselaer Polytechnic Institute, Troy, New York; and [¶]Department of Mechanical Engineering, University of Maryland, College Park, Maryland

ABSTRACT   We find evidence for a direct transition of insulin monomers into amyloid fibrils without measurable concentrations of oligomers or protofibrils, suggesting that fibrillogenesis may occur directly from assembly of denaturing insulin monomers rather than by successive transitions through protofibril nuclei. To support our finding, we obtain size distributions using electrospray differential mobility analysis (ES-DMA), which provides excellent resolution to clearly distinguish among small oligomers and rapidly generates statistically significant size distributions. The distributions detect an absence of significant peaks between 6 nm and 17 nm as the monomer reacts into fibers—exactly the size range observed by others for small-angle-neutron-scattering-measured intermediates and for circular supramolecular structures. They report concentrations in the nanomolar range, whereas our limit of detection remains three-orders-of-magnitude lower (<5 pmol/L). This finding, along with the lack of significant increases in the β-sheet content of monomers using circular dichroism, suggests monomers do not first structurally rearrange and accumulate in a β-rich state but react and reorganize at the growing fiber's tip. These results quantitatively inform reaction-based theories of amyloid fiber formation and have implications for neurodegenerative, protein conformation ailments including Alzheimer's disease and bovine spongiform encephalopathy.

INTRODUCTION

The molecular rearrangement of soluble proteins into insoluble fibers is a common attribute of more than 20 diseases including Alzheimer's disease, Parkinson's disease, spongiform encephalopathies (including mad cow disease), and other prion diseases (1–8). The proteins at their origin take the appellation "amyloid" due to the superficial resemblance between the insoluble fibers they form and starch (Latin: amylum) fibers. The temporal evolution of individual proteins into fibers can be followed optically (e.g., visible ultraviolet spectroscopy (UV-vis) at long wavelengths, birefringence with staining, etc.) as depicted in Fig. 1 A. The profile in the figure, which is characteristic of fibrillogenesis in all these diseases, depicts a lag-time followed by a rise in absorbance and eventually a plateau. For insulin in acetic acid buffer with pH of 2.1 incubated at 65°C, the time-lag is ~25 h (see Fig. 1 A) (9,10). During the early portion of the rise, insulin molecules begin to form fibers. Yet, how exactly amyloid proteins develop into fibers remains unclear.

One school of thought holds that individual molecules (monomers) denature in solution first and then add directly to a growing fiber, perhaps generating synaptotoxic dimers and trimers as reactive intermediates. Shankar et al. (11) isolated these soluble intermediates (i.e., dimers and trimers) of Aβ in samples of human brains from soluble monomers and insoluble fibers and injected them into rats. Those that received

the dimers developed symptoms characteristic of Alzheimer's disease whereas the others did not. An alternate line of inquiry suggests that individual protein molecules form into oligomeric structures that act as nuclei for fiber formation. Examples of these 13-nm to 23-nm-sized structures were reported by Quist et al. (12) for several disease-related proteins. This explanation is appealing, because it provides a mechanism for neurodegenerative diseases. Some of these oligomeric structures may act as ion pores when they fuse with the neuronal cell membranes. Electrical signals transiting the neuron then attenuate due to electrolyte leakage, disrupting signal transduction and giving rise to cognitive disorders (13).

Although detecting soluble oligomers is essential to sorting between these mechanisms, it remains difficult at low concentrations, small size scales, and early times. Previous instruments used to probe the monomers and oligomers include cryo transmission electron microscopy, atomic force microscopy (AFM), and small-angle neutron and x-ray scattering (14–17). A highlight of a recent small-angle neutron scattering study showed a distinct jump in the kinetics when the ensemble size reached a radius of gyration of 3.9 ± 0.2 nm (equivalent to an external diameter of 9.5 ± 0.5 nm), providing further corroboration of a critical nucleus composed of six monomers (14,15). Although these techniques (including optical ones) add valuable information, they are either: not quantitative without extensive standards and calibration; fail to provide a complete size distribution; may present anomalous results as protein conjugates interact with and dry onto substrates; or demand
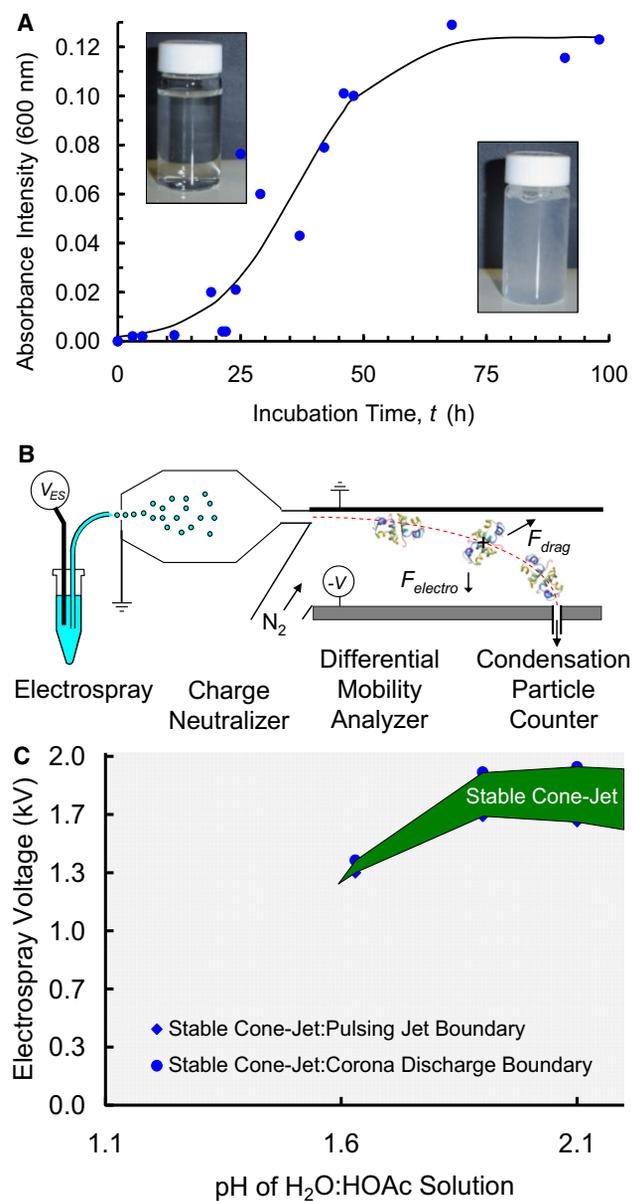
A

B

C

FIGURE 1 Temporal evolution of individual proteins into fibers and measurement method. (A) Absorption intensity at 600 nm versus incubation time at 65°C for insulin samples prepared at 2 mg/mL in 25% acetic acid, pH 2.1. A sigmoidal curve fits the data and guides the eye. (*Insets*) Insulin solution turns opaque as fibers form. (B) Diagram of ES-DMA measurement system (not to scale) consisting of electrospray to produce highly charged, aerosolized droplets; a charge neutralizer to reduce the charge on the drying proteins to +1, 0, or −1; a differential mobility analyzer to separate positively charged particles based on their charge-to-size ratio; and a condensation particle counter to individually count size-separated particles. The panel depicts a dimer adopting several orientations on its trajectory through the DMA. (C) Electrospray voltage versus pH of an acetic acid solution with sheath gas flow rate of 1.2 L/min. The stable cone-jet flow region, with acceptable operating region for the electrospray portion of the ES-DMA system (*green*).

painstaking and time-consuming efforts to provide statistical confidence. In addition, none of these techniques has convincingly demonstrated that nuclei convert into fibers,

although many experimental and theoretical reaction models have assumed this to occur.

Electrospray differential mobility analysis (ES-DMA) provides unparalleled resolution to clearly distinguish among small oligomers and rapidly generates statistically significant size distributions (18–20). We have previously used ES-DMA (see Fig. 1 B) to characterize weakly bound antibody aggregates, distinguishing monomers, dimers, trimer, tetramers, pentamers, and higher-order aggregates with a lower limit of detection of 1.2 nmol/L (18). These oligomers spanned 8–16 nm in size, approximately the size of the oligomers observed by Quist et al. (12) on substrates.

Here we examine insulin as our model of amyloid fibrillo-genesis. Fifty-one amino acids comprise the insulin monomer, the fibrillation of which has been associated with clinical pathology (9,10). For example, insulin fibers have been found on the arterial walls of type II diabetes patients. Additionally, during the preparation of recombinant insulin for clinical use, it may be subjected to low pH, high ionic strength, high shear, or organic solvents—all conditions that may be conducive to fibrillation. Thus, patients who receive continuous subcutaneous insulin infusions with micropumps and repeated insulin shots may experience injection-localized amyloidosis. Insulin also aggregates during the production, storage, and delivery steps, raising concerns for the biotech companies that develop it. In the remainder of this article, we seek to understand the fibrillation process, identifying and kinetically tracking the supramolecular structures formed with circular dichroism (CD) and ES-DMA.

MATERIALS AND METHODS

Buffer selection

Previous studies of insulin have shown that acidic pH, heat, and agitation induce its fibrillation. For example, fiber formation proceeds rapidly at 2 mg/mL, pH 1.6, and 65°C in 100 mmol/L of NaCl and 25 mmol/L of HCl (9,21). Here, we incubate samples of insulin at 65°C in a 25% acetic acid in water solution at pH 2.1 and a concentration of 2 mg/mL to accommodate the electrospray's conductivity window and the need for volatile buffer ions (see Fig. 1).

The overlap of CD spectra in Fig. S1 in the Supporting Material shows that changing the solvent does not adversely impact the three-dimensional structure of the protein, confirming the FTIR results reported by Nielsen et al. (22). It does, however, significantly decrease the rate of fibrillogenesis from 3 h for the onset of fibrillation in a NaCl/HCl solution at pH 1.6 (9,14) to ~25 h in 25% acetic acid at pH 2.1. This result agrees with the trend noticed by Whittingham et al. (23), who found the rate of fibrillation in acetic acid to be significantly retarded relative to that in hydrochloric acid. Nielsen et al. (22), Ahmad et al. (24), and Hua and Weiss (25) also point out that the fibrils formed are noticeably different, even though insulin has similar association states in the different buffers: Insulin is a monomer in 20% acetic acid and a mixture of monomer and dimer in inorganic acids.

Circular dichroism

Samples analyzed by CD were collected during the kinetics experiments (2 mg/mL incubated at 65°C) in 1), 100 mmol/L of NaCl and 25 mmol/L

of HCl at pH 1.6, and 2), 25% acetic acid at pH 2.1), centrifuged at 12000 rpm for 10 min to remove insoluble fibers, and diluted in deionized water. The dilution in deionized water instead of buffer did not affect the spectrum of insulin (data not shown) and allowed us to record a complete CD spectrum from 250 to 190 nm, while with the buffer 200 nm would have been the lowest wavelength possible. CD spectra were obtained at ambient temperature on a model No. 815 spectrophotometer (JASCO, Easton, MD) using a 0.1 cm cell from 250 to 190 nm. For each spectrum, a representative average of four scans was obtained using a data pitch of 0.2 nm, a bandwidth of 1.0 nm, and a scanning speed of 100 nm/min. CD spectra of the appropriate buffers were recorded and subtracted from the protein spectra. The molar ellipticity, θ, was calculated as

$$\theta = \frac{\theta_{CD}M_w/AA}{10\,\delta\,c},\qquad(1)$$

where θ_{CD} is the CD signal (in mdeg), AA the number of amino acids (51 in insulin), δ the path length of the cell (0.1 cm), and c the concentration of the protein (0.1 mg/mL).

Electrospray differential mobility analysis

Size distributions were obtained using ES-DMA from samples prepared at 2.0 mg/mL incubated at 65°C in 25% acetic acid (by volume) for times ranging from 3 h to 139 h. After incubation, the samples were diluted to 50 μg/mL also in 25% acetic acid. The pressure-driven electrospray system was used to sample aqueous solutions of soluble oligomers and short fibrils, producing highly charged droplets which contain them. The electrospray was operated in the stable cone-jet regime with a sheath flow rate of 1.2 L/min (1.0 L/min of air and 0.2 L/min of CO_2). Fig. 1 C maps the conditions under which a stable cone-jet can be maintained, governing our selection of incubation conditions at pH 2.1. A single bipolar neutralizer was positioned between the electrospray and the differential mobility analyzer. The droplets that pass into the neutralizer dry as they collide with both positively and negatively charged gas species (Fig. 1 B).

The dry proteins and protein assemblies exiting the neutralizer have a charge distribution dominated by +1, neutral, and −1 charge states as described by Wiedensohler (26). Using two neutralizers results in a limit of detection nearly two-orders-of-magnitude higher (18). Within the differential mobility analyzer, these dry proteins are exposed to electrical and drag forces. The two forces govern the aerosolized protein's trajectory, such that those with the right charge-to-size ratio (the drag force scales with size) pass via a collection slit at the end of the differential mobility analyzer (DMA) into a single particle counter. Flow through the DMA was set to 30 L/min of nitrogen where higher resolution was advantageous and to 10 L/min where analysis of larger sizes proved necessary. Within the DMA, the applied electrostatic potential ranged from 0 to −11 kV. In the counter, termed a condensation particle counter (CPC), the size-selected proteins act as heterogeneous nuclei, producing micron-sized butanol droplets that are electronically enumerated as they pass in front of a laser beam.

The entire system operates near atmospheric pressure, avoiding the severe pressure drops that can fragment macromolecular conjugates usually associated with electrospray ionization (i.e., like that used in mass spectrometers operated at high vacuum). Data points were collected at a rate of 3/min with a step interval of 0.2 nm. Conversion from mobility diameter to length was achieved using expressions developed in detail by Pease et al. (27) and Kim et al. (28), with a fiber diameter of 8.0 nm. Because the DMA only counts positively charged particles, the raw CPC count is divided by the fraction of positively charged particles described by Wiedensohler to obtain the count for all particles regardless of their charge state when entering the DMA (26). An overlap correction was employed because the DMA may bin particles of the same size at two neighboring voltages. We recently developed a correction, f_{no}, to account for this overlap, which is essential to determining the true concentration.

At 30 L/min, $f_{no} = 1$ for $d \leq 5.2$ nm and $f_{no} = 10.94/d - 29.94/d^2$ for $d > 5.2$ nm, while at 10 L/min of sheath flow, $f_{no} = 3.88/d - 3.58/d^2$ for $d > 2.4$ nm and $f_{no} = 1$ for $d \leq 2.4$ nm (29).

The portion of the spectrum attributable to each type of peak (e.g., monomer, fibers, etc.) is determined and the sum of all corrected counts corresponding to the peak is determined. To determine the free insulin counts, the counts in the dimer peak were multiplied by two, those in the trimer peak were multiplied by three, etc., and the total counts from monomer, dimer, and trimer were summed. Fiber counts are the sum of all overlap-corrected counts attributable to fiber >15 nm.

Atomic force microscopy

Images of insulin fibrils were obtained with an atomic force microscope (MFP-3D; Asylum Research, Santa Barbara, CA) and standard Si cantilevers (AC240TS; Olympus America, Center Valley, PA). Each sample was diluted 1:100 with deionized water and then an aliquot of 20 μL was placed on a mica surface for adsorption for 5 min. Nonadsorbed protein was washed away with deionized water. Three-dimensional measurements were collected in air using the tapping mode technique of AFM. Images were printed and then analyzed. The histogram bins were chosen to complement uncertainty in the measurement implement.

Size calculations

Calculation of size was performed in Mathematica (Wolfram Research, Champaign, IL) (18). The x, y, and z coordinates were downloaded from RCSB Protein DataBank files (PDB) (23,30–34). To accelerate the calculations, the coordinates were digitized by rounding all coordinates to 0.5 Å units. Adopting the formulas given in Pease et al. (18), three orthogonal projected areas were calculated for each configuration of the insulin molecules. This is done by projecting the centers of the atoms onto the grid with 0.25 Å^2 tiles. Because the atoms have a finite size, the van der Waals radius of an average atom in the protein was calculated. At ~1.31 Å, it is very similar to the average radius for atoms in antibodies, suggesting that this strategy is satisfactory for most proteins. A square-tiled pattern of 5×5 square units was then projected for each atom so that each atom was projected over the required 6.25 Å^2 area. Then the number of nonzero tiles corresponds to the final projected area. Because coordinate structures for the monomer were not readily available, the RCSB PDB structure for the dimer was used and the two largest projected areas were divided by two to approximate the monomer.

RESULTS

Structural identification in ES-DMA

Here we examine in detail the conversion of insulin into fibers, collecting size distributions at various times. Fig. 2 A displays distributions with peaks at 2.8 nm, 3.6 nm, and 4.2 nm. To identify each of these structures, we follow Pease et al. (18,20), who calculated the size of antibody aggregates using structures from the RCSB Protein DataBank (23,30–34). In their method, they use the PDB's atomic coordinates to calculate three orthogonal projected areas. Examples of the three projections and their corresponding areas, A_i, are captured in Fig. 3 for the insulin monomer and hexamer. As the insulin adopts a new orientation with every Brownian collision (see Fig. 1 B), the projected areas may be averaged to determine the mobility diameter,
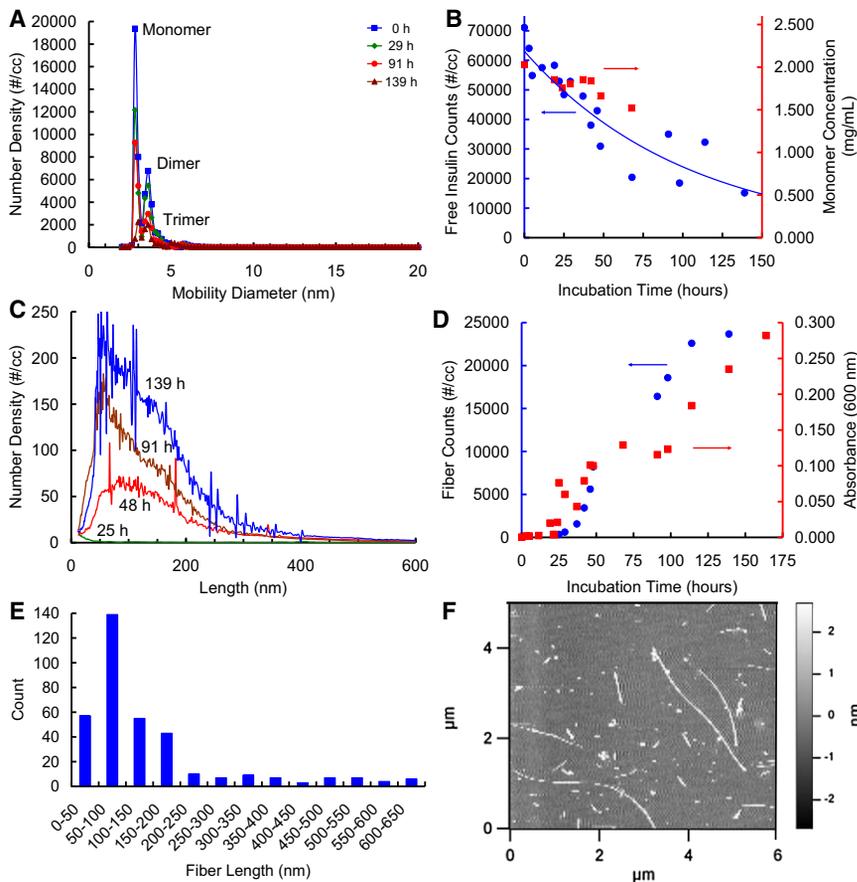
FIGURE 2 The conversion of native insulin into amyloid fibrils. (*A*) Mobility size distribution (i.e., number of particles versus their spherically equivalent diameter) for 2 mg/mL of insulin in 25% acetic acid (pH 2.1) heated to 65°C for the time specified in the legend and then diluted by 40× (0.05 mg/mL) in 25% acetic acid for analysis. DMA operated at 30 L/min of sheath flow. (*B*) Free insulin counts, C_I, from ES-DMA (*circle*) and concentration of free insulin via UV-vis at 280 nm (*square*) versus incubation time, *t*. An exponential curve, $C_I = 6.3 \times 10^4$ (particles/cc) $\exp(-9.7 \times 10^{-3} \, t/h)$, fits the data. (*C*) Length distribution of the same acquired at 10 L/min assuming the insulin fiber to be a rigid rod with a diameter of 8.0 nm as indicated in the AFM. (*D*) Count of insulin fibers from ES-DMA (*circle*) and absorbance/scattering at 600 nm (*square*) versus incubation time. (*E*) Histogram of lengths of insulin fibers captured by AFM in panel *F* binned in 50-nm increments. (*F*) Atomic force microscopy image of insulin fibrils deposited after incubation for 164 h.

$$d_m = \left(\pi^{1/2} \sum_i A_i^{-1/2} / 6 \right)^{-1}, \qquad (2)$$

so termed because it is compared with the diameter found experimentally by determining the gas-phase electric mobility of the protein through the DMA. Although d_m is a spherically equivalent diameter, Eq. 2 accounts for the inherent structure of the insulin molecule through the projected areas. Via this equation, we predict the monomer to have a mobility diameter of 2.75 nm (30,31), the dimer to be 3.45 nm (23,32), and the trimer to range between 3.9 nm and 4.2 nm, depending on the spatial configuration of the individual insulin molecules comprising it, as summarized in Table 1. The agreement between the measured and predicted sizes allows us to identify the peaks as labeled in Fig. 2 *A*.

The PDB structures for the monomer and hexamer are derived from NMR and each contain 10 sets of atomic coordinates representing configurations of similar likelihood. We can use these to estimate the impact of conformational variability on the prediction of mobility size. We find the predicted sizes for the monomer range from 2.72 nm to 2.81 nm and the hexamer to range from 5.14 nm to 5.28 nm. This result indicates that variability in the molecular configuration constitutes less than half of the width of

the peak (0.6 nm at its base) in Fig. 2 *A*, with the remaining uncertainty being contributed by the instrument.

Monomer concentration

Not all multimers in an ES-DMA size distribution necessarily exist in the solution before electrospraying. Pease et al. (18) assert that multiple independent proteins may collect in a single electrospray droplet and dry into an apparent multimer, even though it did not exist in the original solution. They show the mass concentration cutoff, M_{cutoff}, above which apparent dimers must form, to be a function of the protein molecular weight, M_w, and droplet diameter, d_{drop}, as

$$M_{cutoff} = \frac{6M_w}{\pi d_{drop}^3 N_A}, \qquad (3)$$

where N_A is Avogadro's number. We have measured the droplet size to be 154 nm using a sucrose solution (see Fig. S2 *A*), and the molecular weight of insulin is 5.81 kDa (23,32). The cutoff concentration for insulin then becomes 5.0 µg/mL. As the cutoff lies a full order of magnitude below our concentration (50 µg/mL), multiple independent proteins may accumulate in a droplet. Apparent multimers may still form below M_{cutoff} but must form above
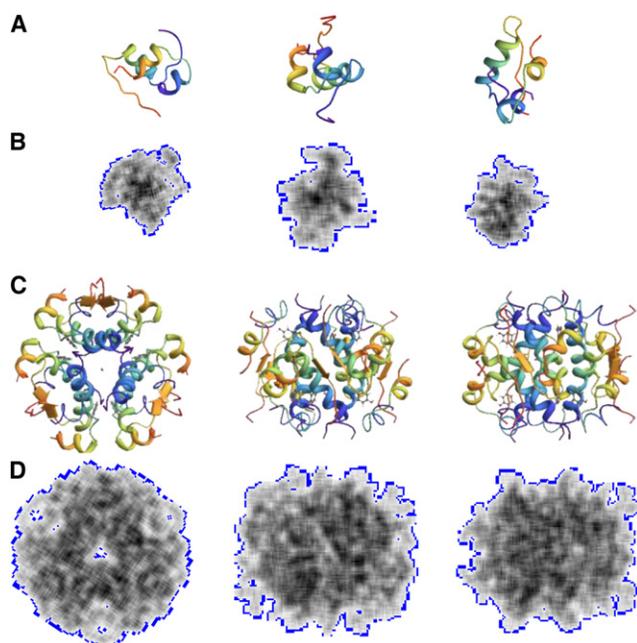
FIGURE 3 Calculating the size of insulin aggregates using structures from the RCSB Protein DataBank. (*A*) Ribbon diagrams for three orthogonal projections of the insulin monomer from the PDB entry 2HIU (30,31). (*B*) Projections used to calculate the projected areas of the insulin dimer with 0.05 nm by 0.05 nm pixels. The calculated areas (from *left* to *right*) are 5.25 nm^2, 6.79 nm^2, and 5.62 nm^2. (*C*) Ribbon diagrams for three orthogonal projections of the insulin hexamer from the PDB entry 1AI0 (33,34). (*D*) Projections used to calculate the projected areas of the insulin hexamer with 0.05 nm by 0.05 nm pixels. The calculated areas (from *left* to *right*) are 22.72 nm^2, 21.32 nm^2, and 20.83 nm^2.

it. Consequently, the dimers and trimers in Fig. 2 *A* must represent, at least partially, apparent dimers and trimers. Decreasing the insulin concentration by dilution decreases the prominence of these apparent species as seen in Fig. S2 *B*.

Apparent dimers cannot be avoided in the current setup because they remained until the lower limit of detection in concentration which we estimate to be 5 pmol/L as indicated in Fig. S3. We note, however, that the ES/neutralizer system does not preferentially ionize monomeric species. Indeed, it preferentially ionizes larger species as indicated by Wiedensohler (26), suggesting that oligomers, if present in appreciable concentrations, would be easier to detect than monomers. (We have accounted for this preferential charging of larger species in figures herein by dividing the

TABLE 1   Identification of key ES-DMA peaks for insulin oligomers

Identification	Predicted size (nm)	Measured size (nm)
Monomer[30, 31]	2.75 ± 0.08	2.8 ± 0.3
Dimer[23, 32]	3.45	3.6 ± 0.6
Trimer (triangular close packed)	3.9–4.2	4.2 ± 0.7
Hexamer[33, 34]	5.20 ± 0.14	Not observed
Hexamer of hexamers arranged annularly	9.9	Not observed

measured number density by the size-dependent probability of charging so that distributions more accurately reflect solution conditions.)

It follows that a strong majority of the insulin in the sample solution not incorporated into a fiber is present in the monomeric state. We can, therefore, elucidate how the concentration of free insulin decreases with incubation time by summing the counts (not integrating) under each peak in Fig. 2 *A*, multiplying the dimer count by two and the trimer counts by three. Fig. 2 *B* shows the total monomer count in solution decreases exponentially in time. An exponential decay is characteristic of a first-order rate equation as expected from fibrillation process (9). The distributions in Fig. 2 *A* are remarkable because they lie at the lower size limit of the instrument (between 1.70 nm and 2.82 nm) (35). Below 5 nm, the CPC does not operate at full efficiency as smaller proteins fail to heterogeneously nucleate droplets within the timescales imposed by the instrument (35,36). This inefficiency prevents final closure of the mass balance. Nevertheless, kinetic trends for the monomer and fiber concentrations may be trusted (see Fig. 2, *B* and *D*).

Fiber concentration

As the free monomer concentration declines, the fiber count increases. Fig. 2 *C*, which plots the aerosol phase number density or count versus the length, shows that the counts attributed to fibers increase with incubation time. In converting from mobility diameter (see Fig. S4 for the mobility size distributions) to length, we followed the model of Kim et al. (28) and Pease et al. (29), who calculate length distributions for multi- and single wall carbon nanotubes using differential mobility analysis. They assume the nanotubes to be rigid rods. Fig. 2 *F* shows that, although the insulin fibers may not be perfectly rigid, the shorter ones do appear to be straight. The model requires the input of a diameter which we take to be 8.0 nm (37,38). The data in Fig. 2 *C* then show that the distribution of long fibers begins to grow between 25 and 37 h and plateaus after 100 h, maintaining an approximately constant width through the duration of fibrillogenesis.

The total counts under the peaks in the length distribution may also be summed and compared to the UV-vis absorbance detected at 600 nm. Fig. 2 *D* shows that the rise in absorbance mirrors the rise in fiber count with incubation time. This agreement is important because it validates the use of UV-vis at 600 nm as a tool to measure the total fiber counts. The UV-vis is valuable because it is rapid and ubiquitously available, though ES-DMA is faster and more informative than competing techniques that provide size distributions including AFM (18).

ES-DMA shows that the length distribution spans sizes from 20 nm long to >400 nm, while the preponderance of the distribution lies between 50 nm and 200 nm in length. This may seem surprising in light of the AFM image in

Fig. 2 *F*, where fibers several microns in length are readily apparent. Careful analysis of the figure, however, indicates the smaller features to be much more numerous, as depicted in the histograms of Fig. 2 *E*. This DMA setup is limited to sizes below ~600 nm (to prevent dielectric breakdown), so the very largest but sparse features in Fig. 2 *F* do not appear in the ES-DMA distributions.

We also examined the incubated samples with CD. The CD spectra represent the configuration of monomers and any soluble oligomers. Before analysis the solution was filtered to remove the larger, less soluble fibers. Fig. S1 *B* shows that the curvature of the spectrum does not change in the range from 210 nm to 225 nm during the course of fibrillation, as might be expected if α-helices in a significant portion of the insulin monomers rearranged into β-sheets. Thus, insulin monomers do not rearrange and accumulate in solution. Previous work by Sethuraman et al. (39,40), with the globular protein, hen egg lysozyme, indicated that inducing misfolding by exposure to a hydrophobic surface (Teflon; DuPont, Wilmington, DE) results in two-phase unfolding kinetics; one phase was very fast (<1 min) with α-helix to random turns' secondary structure, while the other phase was much slower (~1200 min) with α-helix to β-sheet transition.

DISCUSSION

Perhaps the most remarkable aspect of this kinetic data is the lack of oligomeric species in the size distributions of Fig. 2 *A* between 5 nm and 16 nm. This is particularly surprising because several models of amyloid fibrillation rely on the presence of oligomers, critical nuclei, or protofibrils. For example, Lee et al. (9) developed a kinetic model of fiber formation, postulating monomers react to form dimers, timers, etc., until a critical nucleus composed of approximately six monomers is achieved. Subsequent fiber growth continues with monomer addition. However, a cluster size of six monomers would appear in ES-DMA at 5.20 nm $\pm$ 0.14 nm (three standard deviations, see also Eq. 2 and Fig. 3), whereas the largest significant peak is the apparent insulin trimer with size of 4.2 nm.

Our data also do not support the hypothesis that an annular structure, similar to an ion pore, plays a significant role in the in vitro kinetics. The ion pore-like annular structures reported by Quist et al. (12) range in size from 13 nm to 23 nm, and we estimate a hexamer of hexamers, similar to the annular structures they report, to be ~9.9 nm in mobility diameter. In contrast, Fig. 2 *A* shows a complete lack of significant peaks between 9 and 20 nm. This may arise either because the path to fibrillation occurs directly from attachment of denaturing insulin monomers to fibrils rather than through successive transitions through protofibril nuclei or because the concentration of these nuclei remains below the lower limit of detection of this instrument. However, Quist et al. (12) reports that the nuclei concentration in physiological conditions exceed the low nanomolar,

while our limit of detection is ~5.0 pmol/L (see Fig. S3), indicating that the latter possibility is unlikely. Indeed, our continuing experiments find very few ion porelike structures with AFM or cryo-transmission electron microscopy.

Our data also provide insight into possible fibrillation mechanisms. The exponential decay of the free insulin (Fig. 2 *B*), sigmoidal rise in the fiber concentration (Fig. 1 *D*), and relatively constant width of the length distribution (Fig. 2 *C*) are characteristic of chain or additional polymerization reactions. It is also significant that the CD data in Fig. S1 *B* do not appear to exhibit secondary structural changes in solution during fibrillation. Indeed, despite the formation of significant quantities of fiber, the β-sheet content does not increase. This suggests that, despite heat and acidic conditions, the insulin does not unravel in the bulk solution. We, therefore, suspect that free insulin adds directly to the tip of growing fibers without assuming intermediate forms.

Although we can clearly distinguish among the association states of the insulin molecules, we cannot with this technique distinguish between apparent and bona fide dimers based solely on size. However, the ability to generate high purity oligomers of amyloid proteins (i.e., dimers, and trimers) with this technique may be advantageous for use in animal or in vitro studies (11). For example, this technique offers the capability to generate dimers without chemical cross linkers or changes in the oxidation state, which may be used to confirm the results of Shankar et al. (11), who found SEC-purified dimers to be sharply synaptotoxic upon injection into rats.

CONCLUSIONS

The results presented here suggest that oligomers attach directly to the ends of amyloid fibrils possibly without passing through a series of intermediate to large oligomer intermediates. They would need to unfold either in solution or on addition to the ends of the insulin fibers where a template structural transition to β-sheet secondary structure occurs. Measurements using ES-DMA and CD are used to follow both size and secondary structural changes with time along the amyloid reaction coordinate.

SUPPORTING MATERIAL

REFERENCES

1. Campioni, S., B. Mannini, …, F. Chiti. 2010. A causative link between the structure of aberrant protein oligomers and their toxicity. *Nat. Chem. Biol.* 6:140–147.

2. Chiti, F., and C. M. Dobson. 2006. Protein misfolding, functional amyloid, and human disease. *Annu. Rev. Biochem.* 75:333–366.

3. Westermark, P., M. D. Benson, …, J. D. Sipe. 2005. Nomenclature Committee of the International Society of Amyloidosis: Report from the Nomenclature Committee of the International Society of Amyloidosis. Amyloid: toward terminology clarification. *Amyloid.* 12:1–4.

4. Kelly, J. W. 1998. The alternative conformations of amyloidogenic proteins and their multi-step assembly pathways. *Curr. Opin. Struct. Biol.* 8:101–106.

5. Dobson, C. M. 2003. Protein folding and misfolding. *Nature.* 426:884–890.

6. Rochet, J. C., and P. T. Lansbury, Jr. 2000. Amyloid fibrillogenesis: themes and variations. *Curr. Opin. Struct. Biol.* 10:60–68.

7. Soto, C. 2003. Unfolding the role of protein misfolding in neurodegenerative diseases. *Nat. Rev. Neurosci.* 4:49–60.

8. Dobson, C. M. 1999. Protein misfolding, evolution and disease. *Trends Biochem. Sci.* 24:329–332.

9. Lee, C. C., A. Nayak, …, G. J. McRae. 2007. A three-stage kinetic model of amyloid fibrillation. *Biophys. J.* 92:3448–3458.

10. Powers, E. T., and D. L. Powers. 2006. The kinetics of nucleated polymerizations at high concentrations: amyloid fibril formation near and above the "supercritical concentration". *Biophys. J.* 91:122–132.

11. Shankar, G. M., S. M. Li, …, D. J. Selkoe. 2008. Amyloid-β protein dimers isolated directly from Alzheimer's brains impair synaptic plasticity and memory. *Nat. Med.* 14:837–842.

12. Quist, A., I. Doudevski, …, R. Lal. 2005. Amyloid ion channels: a common structural link for protein-misfolding disease. *Proc. Natl. Acad. Sci. USA.* 102:10427–10432.

13. Marx, J. 2007. Alzheimer's disease. Fresh evidence points to an old suspect: calcium. *Science.* 318:384–385.

14. Nayak, A., M. Sorci, …, G. Belfort. 2009. A universal pathway for amyloid nucleus and precursor formation for insulin. *Proteins.* 74:556–565.

15. Vestergaard, B., M. Groenning, …, D. I. Svergun. 2007. A helical structural nucleus is the primary elongating unit of insulin amyloid fibrils. *PLoS Biol.* 5:e134.

16. Nettleton, E. J., P. Tito, …, C. V. Robinson. 2000. Characterization of the oligomeric states of insulin in self-assembly and amyloid fibril formation by mass spectrometry. *Biophys. J.* 79:1053–1065.

17. Dathe, M., K. Gast, …, B. Mehlis. 1990. Insulin aggregation in solution. *Int. J. Pept. Protein Res.* 36:344–349.

18. Pease, 3rd, L. F., J. T. Elliott, …, M. J. Tarlov. 2008. Determination of protein aggregation with differential mobility analysis: application to IgG antibody. *Biotechnol. Bioeng.* 101:1214–1222.

19. Pease, 3rd, L. F., D. I. Lipin, …, A. P. Middelberg. 2009. Quantitative characterization of virus-like particles by asymmetrical flow field flow fractionation, electrospray differential mobility analysis, and transmission electron microscopy. *Biotechnol. Bioeng.* 102:845–855.

20. Pease, L. F., D. H. Tsai, …, M. J. Tarlov. 2007. Quantifying the surface coverage of conjugate molecules on functionalized nanoparticles. *J. Phys. Chem. C.* 111:17155–17157.

21. Nielsen, L., R. Khurana, …, A. L. Fink. 2001. Effect of environmental factors on the kinetics of insulin fibril formation: elucidation of the molecular mechanism. *Biochemistry.* 40:6036–6046.

22. Nielsen, L., S. Frokjaer, …, J. Brange. 2001. Studies of the structure of insulin fibrils by Fourier transform infrared (FTIR) spectroscopy and electron microscopy. *J. Pharm. Sci.* 90:29–37.

23. Whittingham, J. L., D. J. Scott, …, G. Guy Dodson. 2002. Insulin at pH 2: structural analysis of the conditions promoting insulin fiber formation. *J. Mol. Biol.* 318:479–490.

24. Ahmad, A., V. N. Uversky, …, A. L. Fink. 2005. Early events in the fibrillation of monomeric insulin. *J. Biol. Chem.* 280:42669–42675.

25. Hua, Q. X., and M. A. Weiss. 1991. Comparative 2D NMR studies of human insulin and des-pentapeptide insulin: sequential resonance assignment and implications for protein dynamics and receptor recognition. *Biochemistry.* 30:5505–5515.

26. Wiedensohler, A. 1988. An approximation of the bipolar charge-distribution for particles in the sub-micron size range. *J. Aerosol Sci.* 19:387–389.

27. Pease, 3rd, L. F., D.-H. Tsai, …, M. R. Zachariah. 2009. Length distribution of single-walled carbon nanotubes in aqueous suspension measured by electrospray differential mobility analysis. *Small.* 5:2894–2901.

28. Kim, S. H., G. W. Mulholland, and M. R. Zachariah. 2007. Understanding ion-mobility and transport properties of aerosol nanowires. *J. Aerosol Sci.* 38:823–842.

29. Pease, 3rd, L. F., D.-H. Tsai, …, M. J. Tarlov. 2010. Packing and size determination of colloidal nanoclusters. *Langmuir.* 26:11384–11390.

30. http://www.rcsb.org/pdb/explore/explore.do?structureId=2HIU. Accessed on Sept 9, 2008.

31. Hua, Q. X., S. N. Gozani, …, M. A. Weiss. 1995. Structure of a protein in a kinetic trap. *Nat. Struct. Biol.* 2:129–138.

32. http://www.rcsb.org/pdb/explore/explore.do?structureId=1GUJ. Accessed on Sept 9, 2008.

33. http://www.rcsb.org/pdb/explore/explore.do?structureId=1AI0. Accessed on Sept 9, 2008.

34. Chang, X. Q., A. M. M. Jorgensen, …, J. J. Led. 1997. Solution structures of the R6 human insulin hexamer. *Biochemistry.* 36:9409–9422.

35. Wiedensohlet, A., D. Orsini, …, M. Litchy. 1997. Intercomparison study of the size-dependent counting efficiency of 26 condensation particle counters. *Aerosol Sci. Technol.* 27:224–242.

36. Mordas, G., H. E. Manninen, …, M. Kulmala. 2008. On operation of the ultra-fine water-based CPC TSI3786 and comparison with other TSI models (TSI3776, TSI3772, TSI3025, TSI3010, TSI3007). *Aerosol Sci. Technol.* 42:152–158.

37. Jansen, R., W. Dzwolak, and R. Winter. 2005. Amyloidogenic self-assembly of insulin aggregates probed by high resolution atomic force microscopy. *Biophys. J.* 88:1344–1353.

38. Serpell, L. C., M. Sunde, …, P. E. Fraser. 2000. The protofilament substructure of amyloid fibrils. *J. Mol. Biol.* 300:1033–1039.

39. Sethuraman, A., M. Han, …, G. Belfort. 2004. Effect of surface wetability on the adhesion of proteins. *Langmuir.* 20:7779–7788.

40. Sethuraman, A., G. Vedantham, …, G. Belfort. 2004. Protein unfolding at interfaces: slow dynamics of α-helix to β-sheet transition. *Proteins.* 56:669–678.